# A new pressure sensor array for normal stress measurement in complex fluids

Anaïs Gauthier, Mickaël Pruvost, Olivier Gamache, Annie Colin

# A new pressure sensor array for normal stress measurement in complex fluids.

Anaïs Gauthier,* Mickaël Pruvost, Olivier Gamache, and Annie Colin
*MIE – Chemistry, Biology and Innovation (CBI) UMR8231, ESPCI Paris, CNRS, PSL Research University, 10 rue Vauquelin, Paris, France*
(Dated: May 5, 2021)

A new pressure sensor array, positioned on the bottom plate of a standard torsional rheometer is presented. It is built from a unique piezo-capacitive polymeric foam, and consists of twenty-five capacitive pressure sensors (of surface 4.5×4.5 mm$^2$ each) built together in a 5×5 regular array. The sensor array is used to obtain a mapping of the normal stresses in complex fluids, which dramatically extends the capability of the rheometer. We demonstrate this with three examples. First, a pressure profile is reconstructed in a polymer solution, which enables the simultaneous measurement of the first and the second normal stress differences $N_1$ and $N_2$, with a precision of 2 Pa. In a second part, we show that negative pressures can also be measured. Finally, we focus on the normal stress fluctuations that extend both spatially and temporally in a shear-thickening suspension of cornstarch particles. We evidence the presence of a unique heterogeneity rotating very regularly. In addition to their low-cost and high versatility, the sensors show here their potential to finely characterize the normal stresses in viscosimetric flows.

## I. INTRODUCTION

Contrary to Newtonian fluids which are fully characterized by their viscosity $\eta$ only, complex fluids exhibit a much diverse behavior. Their micro-structure, at an intermediate length scale between the molecule and the sample size (the radius of gyration of polymer coils in polymer solutions or the size of solid particles in suspensions) is altered by the flow. This often induces a non-linear relation between the applied stress $\sigma$ and the resulting flow velocity: its understanding is a fundamental challenge, central in many industrial processes. A striking example is the presence of normal stresses, appearing in the diagonal components of the stress tensor. In polymer melts and solutions, the normal stresses are responsible for a number of spectacular effects, such as the swelling of the fluid in extrusion processes, or its climbing on rotating rods [1], and have been the object of numerous studies [2–7]. Normal stresses are much less documented in other systems, even if they are essential to fully characterize the flow of complex materials. Yield-stress fluids, for example develop moderate normal stresses in shear, which sign (positive or negative) and origin are still actively discussed [8–10]. In suspensions of solid particles, the sign of normal stresses is also the object of debate [11–16]. They are causing, in particular, particle migration [17] or edge fracture [18, 19]. The normal stresses also increase dramatically in dense shear thickening suspensions: very high normal stresses, up to 10 000 Pa have been reported [20, 21]. They are often associated with with an inhomogeneous flow, and generate localized forces strong enough to damage the rotors of mixing systems [21].

In viscosimetric flows, normal stresses are far less studied than shear stresses, mostly because their measurement is not straightforward. Indeed, on a torsional rheometer, the normal stress differences $N_1$ and $N_2$ are usually measured by combining two experiments with different geometries: the net thrust force gives access to $N_1$ in a cone/plate geometry, and to $N_1 - N_2$ in a parallel plate geometry [1, 10, 13, 22, 23]. $N_2$ is then calculated by finding the often small difference between two large experimental quantities, which amplifies the impact of any measurement error [7]. Other techniques have been developed to obtain a more reliable measurement of $N_2$ [3, 13], or to avoid using a cone plate geometry (unsuitable in some systems such as suspensions of large particles): the rotating rod rheometry [11, 17, 24, 25], the measurement of the shape of a free surface [3] or the tilted through method [12, 26]. Another method consists of measuring the pressure distribution as a function of the radial position $r$ in a cone/plate or a plate/plate geometry, by using a small number of pressure sensors integrated to the plate of a torsional rheometer. This technique, which gives both $N_1$ and $N_2$ in a single experiment, has been attempted in polymer solutions [2, 4, 7, 27] and recently in a non-Brownian suspension [14].

Unfortunately, such setups are complex to build and measurements can be flawed. For example, Couturier *et al.* [12] use a rectangular channel that causes unwanted secondary flows near the corners of the cross-section. The use of sensors must also meet a number of important requirements, for example being small enough relatively to the rheometer plate, be extremely sensitive and not cause any disturbance to the flow [28]. The pressure transducer membranes have to be positioned at exactly the same level as the disk surface: if not, a hole pressure has to be accounted for [29, 30], and may lead to error measurements, as in the pioneering work of Adams and Lodge [2]. To this purpose, Dbouk and coworkers [14] coated the surface transducers with paraffin, so that no pressure hole effect is expected to take place. In addition, the number of sensors is often limited by the size of the plate and by the volume of the acquisition system.

Here, we demonstrate the potential of a new low-pressure sensor array in the measurement of normal stresses in non-Newtonian fluids, with a spatial resolution of 4.5×4.5 mm$^2$. The number of sensors (25 in a 4×4 cm$^2$ surface), their precision (up to 2 Pa for pressures below 1000 Pa) and the frequency of measurements (200 Hz) are unprecedented. In ad-

* anais.gauthier@espci.fr

dition, the sensor array is highly versatile: the position, the size and the number of sensors is easily varied by changing the bottom electrode only. They also do not drift with time, and involve no pressure hole as the contact surface is flat and made of one piece. After presenting the sensor fabrication method and acquisition system, we demonstrate its potential to characterize three different flows, in a parallel plate geometry. First, in a polymer solution, we measure simultaneously the two normal stresses $N_1$ and $N_2$, both in very concentrated and very diluted systems. We then focus on a Newtonian fluid subjected to a secondary flow, and measure this time negative pressures. Finally, we consider a shear-thickening fluid which exhibits flow heterogeneities: our sensors evidence the presence of a single aggregate rotating very regularly, an intriguing phenomenon that cannot be detected through the force sensor of the rheometer.

## II. THE SENSOR ARRAY: FABRICATION, CALIBRATION AND PROPERTIES

### A. Sensor array

A distinctive feature of the pressure sensor array presented here is that the 25 sensors are not designed individually. As shown in figure 1a, the sensor is made of two surfaces: a solid *electrode network* (left) and a soft *measurement surface* (right) made of a polymeric material. As shown in Figure 1b, the electrode network is placed on the bottom plate of a torsional rheometer (Discovery HR-2, TA instruments) and covered by the measurement surface. A thin grid of double sided tape is added between the two surfaces. The 3-layer sandwich thus formed is the pressure sensor array itself, with a total thickness of $\sim 3$ mm. It is presented in sectional view in Figure 1c.

The bottom layer is shown in dark blue and gray. It is a simple electrode network, custom-made by JLC PCB. The electrodes are 25 conductive square surfaces of $4.5\times4.5$ mm$^2$, organised in a 5 by 5 regular matrix, and connected individually to the acquisition system. The total surface of the network is $4\times4$ cm$^2$, which corresponds to the typical size of a rheometer plate geometry.

On top of the electrode network is attached a 25 μm thick layer of double-sided tape, shown in green in Figure 1c. Using a laser cutter, 25 square holes (with size $5\times5$ mm$^2$) are cut into the tape so that it does not cover the electrodes. The role of this intermediate layer is double: first, it ensures a good adhesion of the bottom layer to the measurement surface. In addition, its presence increases the sensitivity of the sensor by a factor 10 at very low pressures ($< 150$ Pa). We interpret this as the consequence of a bending of the soft measurement surface within the grid (by typically 10 to 20 μm) which can only happen when the measurement surface is slightly raised above the bottom electrodes.

The last layer is the measurement surface itself. Its core is a piezo-capacitive soft solid foam (shown in black in Figure 1c), made from a polydimethilsiloxane polymer (PDMS) filled with 10% in weight of carbon black particle. This material was developed previously in our team, and its fabrication method is presented in detail in Refs. [31, 32]. Here, the solid foam is fully integrated into a multi-layered sandwich to make a solid and reliable sensor. The foam itself is prepared as described in [32], through a water-in-oil emulsion process: a mixture of water and carbon-black particles is slowly added to PDMS, under vigorous mixing. The emulsion then forms a paste, that is uniformly spread in a 1 mm thick sheet using an applicator (Zehntner ZUA 2000). The spreading is done on a Mylar surface covered by an 5 μm thick insulating layer of plain PDMS (shown in yellow in Figure 2c), previously deposited with a spin-coater and cured for 1h at 70°C. After spreading, the paste is cured in a two-step process. First, it is placed in a bath of deionized water at 70°C for 6 h to ensure cross-linking of the PDMS polymer. After curing, the solid is let to dry at 70°C for 24 h so that all water contained in the pores evaporates. After curing and drying, the emulsion turns into a piezo-capacitive soft solid foam. Its relative softness (with a Young modulus of 1.6 MPa [31]) is at the source of its remarkable piezo-capacitive properties: when a pressure is applied on the material, the micropores (of size between 1 and 10 μm) deform, which induce a large variation of its permittivity and thus its capacitance. In the sensor array, the upper part of the foam is covered by a 25 μm thick paste of silver particles (Creative Materials), shown in gray in Figure 1c, which plays the role of a soft electrode. The upper electrode is connected to the acquisition system by planting a conductive screw attached to a wire through the silver film (as in Figure 1a). Finally, a protective coating of PDMS is cast around the three layers of the measurement surface. The PDMS, initially liquid, is let to rest for 30 min at ambient temperature to ensure that the measurement surface is flat. It is then cured at 70°C for 1h. We thus obtain a good alignment of the sensor with the upper plate geometry. Small fluctuations of the thickness (of the order of 20 μm) are observed when determining the zero position of the upper plate. These perturbations are small compared with the gap size in our experiments (1 mm) and the radius of the geometry (2 cm) and they are considered as standard in rheology.

The Young modulus of the whole measurement surface is close to the modulus of the piezo-capacitive foam alone ($\simeq 1.6$ MPa [31]). At small pressures (of the order of 100 Pa), the main source of deformation of the sensor originates in its local bending in the grid of double-sided tape. The level difference between the disc and the coated sensor is thus less than 25 μm, while the gap between the discs is set to 1 mm. In such conditions, no pressure hole effect is expected. To check if the softness of the sensor and the small thickness variations of the measurement surface might impact the flow, we compare in Supplementary Figure 1 the flow curves of the two non-Newtonian fluids studied here (a polymer solution and a cornstarch suspension) when measured directly on the (solid) rheometer plate or on the soft sensor array. In both cases, the flow curves are almost identical, which indicates that the presence of the sensor does not significantly disturb the flow.

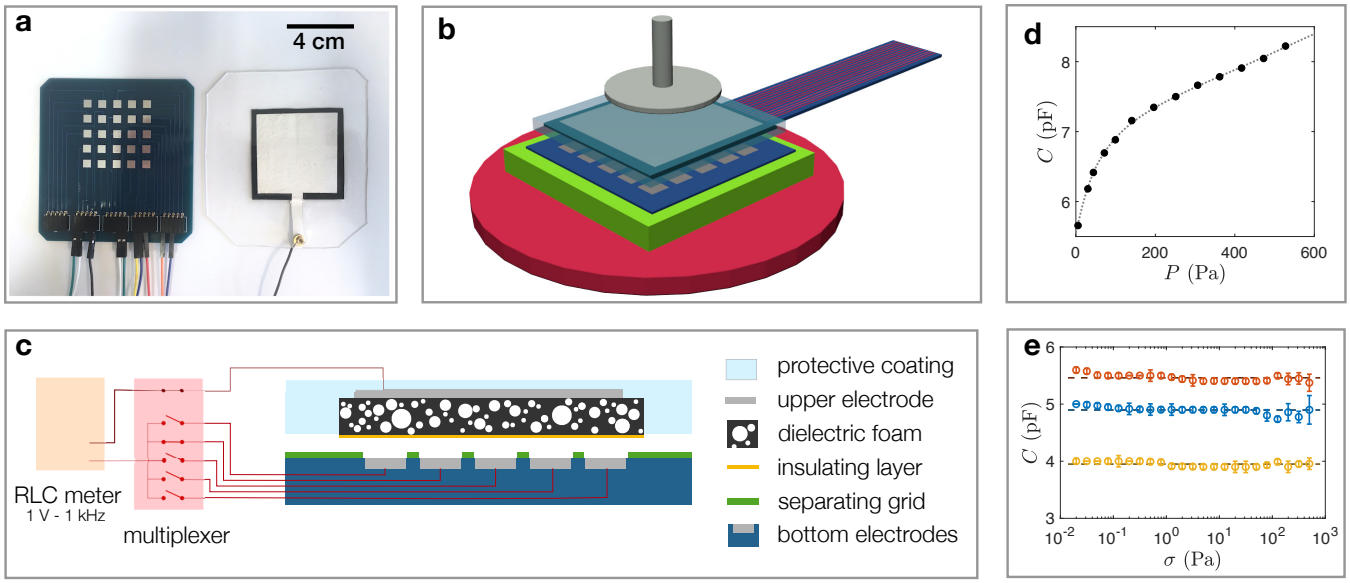


FIG. 1. **a.** Picture of the electrode network (left) and the measurement surface (right) of a sensor array. **b**. Experimental system: both layers are placed on top of each other on the bottom plate of a parallel plate rheometer. The upper disk has a radius $R$ of 2 cm, and the gap thickness $h$ is 1 mm. **c**. Side-cut of a capacitive sensor array. **d.** Typical calibration curve of one sensor for applied pressures $P > 0$, showing the capacitance $C$ as a function of a hydrostatic pressure $P$. **e.** Capacitance of three sensors when subjected to varying shear stress $\sigma$. Blue dots correspond to a central sensor (at a position $r = 0$ to the center of the geometry) while the red and yellow dots correspond to two sensors positioned diagonally at $r = 12$ mm.

### B. Acquisition system.

Due to its softness, the measurement surface does not redistribute the pressure and the three-layers sandwich sensor array behave as 25 independent piezo-capacitive elements. Their capacitance $C$ (varying typically between 3 and 10 pF) is directly correlated to the local pressure. Each sensor capacitance $C$ is recorded as a function of time by an acquisition system, schematized in Figure 1c. It consists of two instruments: a multiplexer (Keysight 34980A Agilent technologies) and a precision LCR meter (Keysight E4980AL Agilent technologies), both controlled using a in-house Matlab code. The LCR meter imposes a sinusoidal signal at low frequency (1 kHz) and low voltage (1 V), and measures the capacitance of the connected circuit with a precision of 0.05 %. Its internal impedance is automatically adjusted to the circuit: here it is set to 5 kΩ. The multiplexer consists of 25 optical switches (one per sensor), with response time 0.2 ms. During a measurement, the following steps are repeated: first, the switch corresponding to one bottom electrode is closed, and the LCR meter records the capacitance of the circuit between this electrode and the top electrode, averaged over 50 ms. The switch is then closed. This protocol is repeated for every sensor of the array – which takes approximately 1.5 s for all 25 sensors – before the next measurement cycle starts. In the following analysis of the data, an internal compensation calculation is done to account for the impedance of the multiplexer and wires. In most experiments, we use between 5 and 10 sensors, which automatically increases the measurement frequency, up to 2-3 cycles per second.

For higher frequency measurements, we use an electronic circuit custom made by Piwio, which miniaturizes the acquisition system. The circuit is similar in principle to the one described above, with three main differences. First, square waves of 1 V amplitude are used, with frequency 1 kHz. Second, there is one multiplexer for every 4 sensors, which increases the measurement frequency. Finally, the capacitance is measured with a low resolution of 0.1 pF, and it is not averaged. This system is much faster than the previous one (up to 200 Hz), but less accurate. In Supplementary Figure 2, the typical response of the sensors when connected to the two acquisition systems are compared. When using the precision LCR meter, the noise (of the order of 1.5 Pa) is higher than the resolution of the acquisition system (0.00001 pF, which corresponds to a pressure of $10^{-3}$ Pa). With this measurement method, pressures as low as 2 Pa can be measured, as further confirmed in Figure 3c. The Piwio integrated board, on the other hand, is limited by its resolution and cannot measure pressures below 10 Pa. These values of 2 and 10 Pa, which set experimentally the pressure detection threshold of our sensors, are close to the 4 Pa threshold of our rheometer (Discovery HR-2, TA instruments). However, since the surface of the sensors is 65 times smaller than the surface of the rheometer geometry, the sensor array is sensitive to forces typically 50 times smaller than the rheometer. It should finally be noted that very low capacities (between 3 and 10 pF) are measured here, so that a non-negligible part of the noise in the measurements comes from stray fields in the lab environment. To limit their impact, we used in all experiments a non-conductive geometry (in PMMA), and we were careful to limit the length of the wiring.

### C. Sensor calibration.

The sensors are calibrated using hydrostatic pressure in compression, and using a well-known flow in extension. In compression, a cylinder (with diameter 6 cm) is placed on top of the measurement surface and made water-tight with grease. Water is then added, and the capacitance $C_i$ of each sensor is measured as a function of the water pressure $P = \rho g h$ (with $h$ the liquid height, $\rho$ water density and $g$ gravity). A calibration curve is presented in Figure 1d: the sensor capacitance $C$, initially equal to a $C_0 = 5.5$ pF, increases by 50% for a pressure variation $\Delta P$ of 600 Pa. The sensitivity $S = \frac{\Delta C/C_0}{\Delta P}$ is higher at low pressures, with $S = 1.8$ kPa$^{-1}$ for $P < 100$ Pa. It remains excellent at higher pressures, with $S = 0.7$ kPa$^{-1}$ for $200\text{ Pa} < P < 1000$ Pa. While the sensors are particularly sensitive to the applied pressure, they do not react to shear stress. This is shown in Figure 1e, where the sensors capacitance is recorded when shearing silicone oil with viscosity 100 000 cSt. At the stresses $\sigma$ considered here, silicone oil is a Newtonian fluid, with a constant viscosity and no measurable normal stress (see Supplementary Figure 3). The response of 3 sensors, placed either at the center of the geometry (blue dots) or at an equal distance $r = 12$ mm to the center (red and yellow dots) is shown. While the applied shear stress $\sigma$ is varied over 5 orders of magnitude, the sensors capacitance remains constant. Finally, the sensors are calibrated in extension using a Newtonian fluid sheared at high velocity. Indeed, in a parallel plate geometry, a recirculation appears, which generates a negative pressure close to the static plate, varying quadratically with the angular velocity $\Omega$ of the rotating plate (see section IV for more details). We use this theoretical pressure value as a reference to calibrate our sensors.

Two other properties of the sensor are also considered. First, we estimated the sensor response time by applying a constant pressure load ($< 1000$ Pa) on the sensors and removing it suddenly. The sensors response time is limited by the dynamical response of the membrane, that deforms under the applied stress. It is of the order of 50 ms when increasing pressures are applied, but it can reach 100 to 200 ms when a high pressure (typically 1000 Pa) is suddenly lifted. Experimentally, we observed an increasing hysteresis when applying pressures $P >$ 3000 Pa, which might correspond to a too large deformation of the measurement surface in the grid. For this reason, we will focus here on pressures between 0 and 1000 Pa, which corresponds to the optimal operating mode of our sensors. In the experiments considered here, the measurement frequency varies between 1 and 20 Hz, so that the pressure is always averaged over a duration that is of the order or larger than the sensor response time. We finally checked that the sensors do not exhibit any significant drift in time. This is demonstrated in Supplementary Figure 4a: the response of the sensors, submitted to a constant hydrostatic pressure of 300 Pa is shown to remain constant. In addition, we compare in Supplementary Figure 4b the sensors response before and after a 2000 s experiment, after being subjected to pressures varying between 100 and 400 Pa. The difference of the pressure measured at zero angular velocity before and after 2000 s is smaller than 4 Pa, which is of the order of the accuracy of the sensors. The potential drift is thus extremely small compared to what is reported in the literature [10, 14], which can reach 15 to 30 Pa in 60s [10].

### D. Rheology procedure.

We use a parallel plate geometry, with the measurement surface of the sensor as a static bottom plate. The rotating disk is made of PMMA (to limit the effet of stray magnetic fields on the sensors) and sanded, with a radius $R = 2$ cm. This geometry was selected in all experiments so that the gap $h = 1$ mm is always much larger than the intrinsic variations in thickness of the measurement surface or its variations due to compression with the normal stresses (which are both of the order of 20 $\mu$m). This geometry thus limits the influence of the measurement surface on the flow: as presented in Supplementary Figure 1, the flows in a parallel plate geometry with and without the sensor are almost identical. The liquid of study is added directly on the measurement surface. After positioning the upper disk at the working gap ($h = 1$ mm) the liquid in excess is carefully cleaned, so that the meniscus at the edge of the plate is as vertical as possible. Since the PDMS covering the measurement surface is smooth and hydrophobic, the contact angle of the fluids used here (water-based solutions, glycerol) is of the order of 90°, as schematized in Figure 2c, and the meniscus is slightly concave. This does not affect the rheological measurements (as seen in Supplementary Figure 1) but it facilitates liquid ejection, which is observed at a lower angular velocity than on the rheometer plate (a rough and hydrophilic solid).

Once the liquid and the geometry are positioned, both the internal force sensor of the rheometer and the sensor array are set to 0. This consists in assuming that the system is pre-stressed by a constant pressure $P_c$ (typically of the order of 50 Pa) due to the meniscus, that is subtracted in the following measurements. This assumption is valid as long as edge effects due to the distortion of the meniscus or instabilities such as edge fracture remain small enough to be neglected. Numerical simulations of situations where instabilities of the meniscus occur is complex. However, there seems to be both a theoretical and experimental consensus on edge fracture [18, 19, 33]. The latter is expected to appear in fluids with a negative second normal stress $N_2$, when $|N_2|$ exceeds a critical value $N_c \simeq 5\gamma/h$, with $\gamma$ the surface tension of the fluid and $h$ the gap size. In our experiments with a polymer solution of HPAM, $N_2$ never exceeds 16 Pa, which is much smaller than $N_c \simeq 350$ Pa. This value is also very large for the particle suspension system, where, in addition, we do not expect edge effects to directly impact our results, focused on the detection of flow heterogeneities. In other situations, such as instabilities induced by inertia (at thus at large shear rates $\dot{\gamma} > 200$ s$^{-1}$) we checked that, in all experiments, the potential pressure variation induced by the increased meniscus deformation at the edge (of the order of 20 Pa) always remains small compared with the mean pressure in the flow.

During an experiment, a constant shear stress $\sigma = \sigma_{12}$ is imposed on the fluid by the upper disk (with radius $R = 2$ cm),

where 1 and 2 are the directions of the velocity and the velocity gradient. The average normal stress is obtained with the built-in force sensor of the rheometer, which measures the mean vertical thrust on the geometry. The sensor array, on the other hand measures the pressure $P(r,\theta) = -\sigma_{22}$ close to each sensor, with $\sigma_{22}(r,\theta)$ the component of the stress deviator tensor (in the $22 = zz$ direction) in the position $(r,\theta,z=0)$. In the parallel plate geometry, we denote $\dot{\gamma}_R$ the shear rate at the edge, and $\dot{\gamma}$ the local shear rate under the plate, with $\dot{\gamma} = \frac{r\Omega}{h}$. For shear rates $\dot{\gamma}_R < 200$ s$^{-1}$, the velocity $\mathbf{v}$ of the fluid is (almost) purely orthoradial, with $\mathbf{v} \simeq v_\theta \mathbf{e}_\theta = r\frac{\Omega z}{h}\mathbf{e}_\theta$, and $v_r, v_z \ll R\Omega$.

For an homogeneous liquid, the equation of motion along the $r$ direction writes:

$$\frac{1}{r}\frac{\partial}{\partial r}(r\sigma_{33}) - \frac{\sigma_{11}}{r} = -\rho\frac{v_\theta^2}{r} + \frac{\partial p}{\partial r} \qquad (1)$$

, where 3 denotes the vorticity direction. Equation 1 can describe two types of flows, that will be characterized separately in sections III and IV. First, we consider the flow of a non-newtonian fluid. For $\dot{\gamma} < 500$ s$^{-1}$, the inertial effects (appearing in the term $\frac{\partial p}{\partial r}$ in Eq. 1) are neglibible compared with the effect of the normal stresses, and this term is neglected. The diagonal components in the stress tensor $\sigma$ generate a radial variation of $-\sigma_{22}$, which is measured by the sensors. In section IV, a Newtonian fluid is sheared at high angular velocities. In this configuration, the fluid does not develop normal stresses and the left-hand side of Eq. 1 is neglibible. The inertial term $\frac{\partial p}{\partial r}$ generates a slow recirculation of the liquid, and a negative pressure profile is measured.

## III. POSITIVE NORMAL STRESS MEASUREMENTS

Long-chain polymer solutions are viscoelastic fluids, which flow is characterized by three functions: their viscosity $\eta = \sigma/\dot{\gamma}$, the first normal stress difference $N_1 = \sigma_{11} - \sigma_{22}$ and the second normal stress difference $N_2 = \sigma_{22} - \sigma_{33}$. In polymer melts and concentrated polymer solutions, $N_1$ is typically positive and high, while $N_2$ is more than 10 times smaller and negative [1].

Using the pressure sensor array, both $N_1$ and $N_2$ are measured in a single experiment. We use a solution of a partially hydrolyzed polyacrylamid polymer (HPAM) with a high molar mass $M_w = 18.10^6$ g/mol. HPAM is a charged linear polymer consisting of acrylamid monomers, where 25 to 30% of the amine group are replaced by a carboxyl group. The concentration of HPAM in water is varied from 200 ppm (very diluted) to 5000 ppm (very concentrated). As shown in Figure 2a, the rheology of these solutions is characteristic of a viscoelastic fluid, with a strong shear thinning: the viscosity $\eta$ decreases with $\dot{\gamma}_R$ following a power law $\eta \propto |\dot{\gamma}_R|^n$. $n$ increases in magnitude with the concentration: on Figure 2a, the best fit (dotted lines) is obtained for $n = -0.84$ for 5000 ppm, $n = -0.70$ for 1000 ppm and $n = -0.65$ for 200 ppm. At high shear rates, the liquid develops normal stresses, which average value is measured by the build-in force sensor of the rheometer, and presented in Figure 2b. The thrust $F_z/\pi R^2$ averaged on the plate surface is plotted as a function of $\dot{\gamma}_R$ for three HPAM solutions. The concentrated solutions exhibit high normal stresses: for example, the mean normal stress of the 5000 ppm solution is more than ten times higher than the shear stress $\sigma$ at high shear. In the region where they are present, the normal stresses increase proportionally to $\dot{\gamma}_R^m$. From Figure 2b, we find $m = 0.41$ for the 200 ppm solution, $m = 0.85$ for the 1000 ppm solution and $m = 0.92$ for 5000 ppm. $m$ is here always smaller than 2 and increases with the concentration, a phenomenon which has already been observed in similar solutions.

The sensors measure the pressure $P = -\sigma_{22}$ as a function of the radial distance $r$ to the center of the geometry, as defined in Figure 2c (top). For simplicity, we present here the pressure measurement of only 5 different sensors placed at varying distances $r$ to the center of the geometry, and distributed in all directions. Indeed, as presented in Supplementary Figure 5, two sensors placed at an identical distance $r$ to the center of the geometry measure the same pressure. On figure 2c, the sensors are colored in blue ($r$ = 3.2 mm), red ($r$ = 6.6 mm), yellow ($r$ = 11.0 mm), purple ($r$ = 14.9 mm) and green ($r$ = 16.0 mm). The geometry is shown in light blue: its center (indicated by a black dot) is placed at the level of the upper right corner of the central sensor.

A typical experiment is presented in Figure 2d, with a 5000 ppm HPAM solution. The shear stress $\sigma$ (plotted on top) is increased by regular steps of 300 s, from $\sigma = 0$ Pa to $\sigma$ = 20 Pa. The stress $P = -\sigma_{22}$ measured by each sensor is recorded as a function of time $t$, and presented in Figure 2d with the same color code as in Figure 2c. As visible in Figure 2d, $P$ increases with $\sigma$. At each stress-imposed step, the higher pressures are measured close to the center of the geometry (in blue): the pressure continuously decreases with $r$. While it remains almost constant for $\sigma \leq 15$ Pa (with a very slight decrease in time), the pressure signal becomes noisy for $\sigma > 15$ Pa. We interpret this as a consequence of an elastic turbulence phenomenon, which are likely to occur at low Reynolds numbers in our systems [34–36]. Such instabilities are driven by the stretching of the polymer chains in the azimutal direction. Following Pakdel and Mc Kinley [37, 38], we expect these instabilities to appear in the a parallel plate geometry when the criterion $(h/R)^{1/2} N_1/\sigma > M$ is met, with $R$ the streamline curvature and $M$ a constant, ranging between 1 and 6 depending on the rheological law of the fluid [39, 40]. Anticipating that $|N_2| \ll N_1$, we calculate the Weissenberg number at the transition as $\mathrm{Wi} = N_1/\sigma \simeq F_z/(\pi R^2\sigma) \simeq 10$, which leads to $M \simeq 3$. This value is in good agreement with what is expected for elastic turbulence [36].

From Figure 2d, the pressure $P(r)$ measured at increasing distances $r$ within the sheared polymer solution are extracted, and plotted for each shear stress $\sigma$. The results are presented in Figure 3a, b and c, where $P(r,\sigma)$ is plotted for varying polymer concentrations (5000 ppm in Fig. 2a, 1000 ppm in Fig. 2b and 200 ppm in Figure 2c). The error bars correspond to the error due to the sensor itself (which is done by comparing the pressures of two sensors placed at an equal distance to

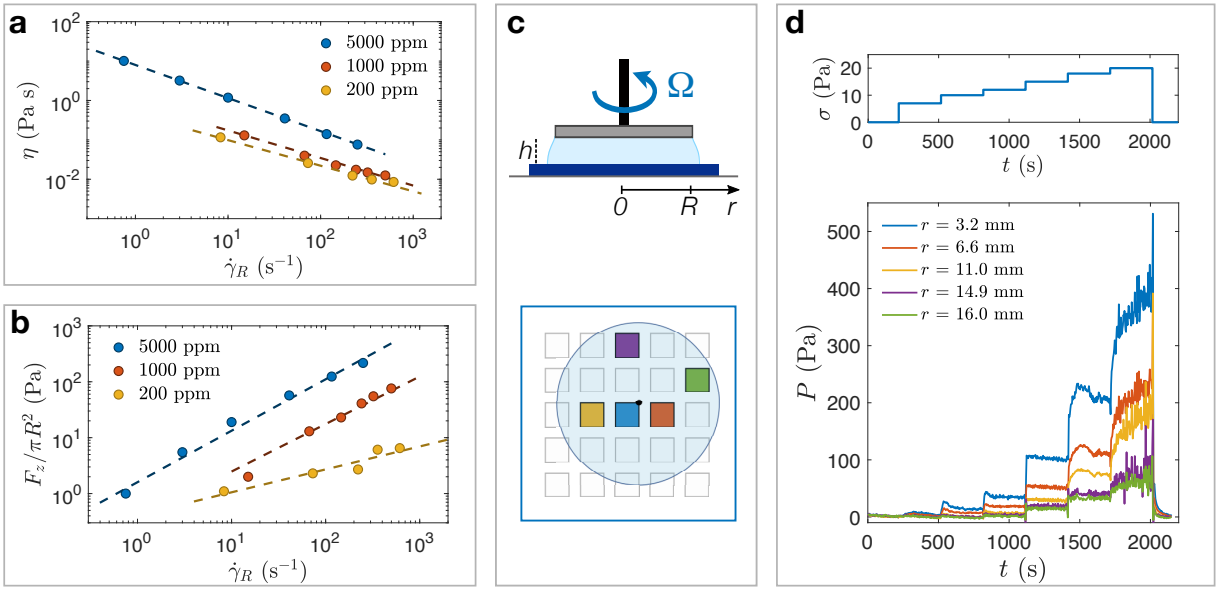


FIG. 2. Rheological measurements of HPAM solutions **a.** Viscosity $\eta$ as a function of the shear rate $\dot{\gamma}$ for three different concentrations of a HPAM solutions: 5000 ppm (blue), 1000 ppm (red) and 200 ppm (yellow). **b.** Average vertical pressure $F_z/\pi R^2$ measured through the built-in sensor of the rheometer, as a function of $\dot{\gamma}_R = R\Omega/h$. **c.** (top) Side view of an experiment. The pressure profile $P(r)$ is measured as a function of the radial distance $r$ to the center of the geometry. (bottom) Top view of the sensor array, with the sensors used in the experiment shown in bright colors. **d.** Response of the sensors during a typical experiment of stress-imposed steps $\sigma(t)$. The pressure $P = -\sigma_{zz}$ measured by 5 different sensors is plotted as a function of time $t$.

the center) and from the noise in the pressure measurements. For all polymer concentrations, the pressure $P$ is positive, and decreases with the distance $r/R$ to the center of the geometry. This is similar to previous observations of Alcoutlabi *et al.* [7] in solutions of a different polymer. The pressure profiles $P(r)$ all seem to extrapolate to a positive pressure for $r = R$, which is consistent with a negative value for $N_2$ [1, 7]. It should also be noted that the pressures detected here are significantly smaller than the ones measured in other polymer solutions [7]. In particular, minute pressures (smaller than 10 Pa) that develop in very diluted solutions (figure 2c) are detected, which opens the way to a better characterization of these much less studied systems.

The experiments are compared with the pressure profile $P(r)$ expected from the theory. Since the sensors are set to zero at the beginning of every experiment, the pressure difference due to the meniscus is already taken into account, so that the pressure measured by the sensors is equal to $-\sigma_{22}$. The effect of centrifugal forces is very small here compared with the normal stresses, so that the inertial term $\partial p/\partial r$ in Eq. 1 is neglected. Finally, using $N_1 = \sigma_{11} - \sigma_{22}$ and $N_2 = \sigma_{22} - \sigma_{33}$, the equation of motion within the fluid (Eq. 1) is expressed as a function of $\sigma_{22}$ and the two normal stresses only [14]:

$$\frac{\partial \sigma_{22}}{\partial r} = \frac{\partial N_2}{\partial r} + \frac{(N_1 + N_2)}{r}. \tag{2}$$

We assume here that in the HPAM solutions, as in many polymer solutions, the two normal stresses are proportional to $\dot{\gamma}^n$[3, 4, 7, 25]. This comes to assume that $N_1$ and $N_2$ can be written as $N_1 = \alpha_1 \dot{\gamma}^n$ and $N_2 = \alpha_2 \dot{\gamma}^n$, with $\alpha_1$ and $\alpha_2$ the normal stress coefficients. In other systems, this hypothesis might not hold: in this case, it is also possible to use our sensors slightly differently to measure $N_1$ and $N_2$, as detailed in the supplementary materials.

Using the expressions of $N_1$ and $N_2$ as a function of $\dot{\gamma}$, and $\dot{\gamma}_R = R\Omega/h$, equation 2 writes:

$$\frac{\partial \sigma_{22}}{\partial r/R} = \dot{\gamma}_R^n \left(\alpha_1 + (n+1)\alpha_2\right) \left(\frac{r}{R}\right)^{m-1} \tag{3}$$

This equation is integrated with respect to $r$. The boundary condition is found assuming that at the meniscus at the edge of the geometry (in $r = R$) the third normal stress is equal to the capillary pressure, which writes $\sigma_{33}(r = R) = -N_2(R) + \sigma_{22}(R) = P_c$, with $P_c$ the capillary pressure [14]. Since all sensors are set to zero at the beginning of the experiment (at zero angular velocity), this pre-load is already taken into account and $P_c = 0$. This gives:

$$P(r) = -\sigma_{22}(r) = -\dot{\gamma}_R^n \left[\frac{\alpha_1 + (m+1)\alpha_2}{m} \left(\frac{r}{R}\right)^m - \frac{(\alpha_1 + \alpha_2)}{m}\right]. \tag{4}$$

The pressure profile $P(r)$ thus varies linearly with $(r/R)^m$. This formula is used to determine the two normal stress coefficients $\alpha_1$ and $\alpha_2$. To do so, we combine all experiments for a given polymer solution and plot $P/\dot{\gamma}_R^n$ as a function of $(r/R)^m$. This is shown in Figures 3a-c for HPAM concentrations of 5000 ppm, 1000 ppm and 200 ppm. The different location of the data on the $r/R$ scale comes from the different positions

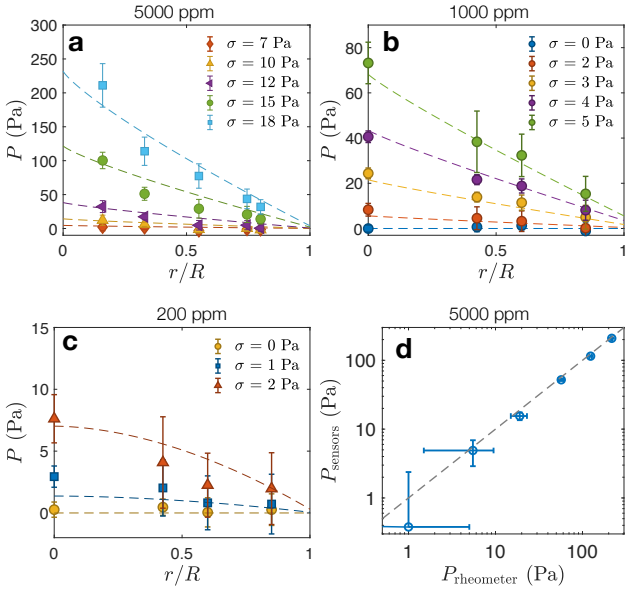


FIG. 3. Pressure profiles $P(r)$ within flowing HPAM solutions in a plate/plate configurations, for varying shear stresses $\sigma$. The dotted lines are the best fit of the model, with $P(r) = -\dot{\gamma}_R{}^m \left[\frac{\alpha_1+(m+1)\alpha_2}{m}\left(\frac{r}{R}\right)^m - \frac{\alpha_1+\alpha_2}{m}\right]$. **a.** Solution of 5000 ppm HPAM in water: $\alpha_1 = 4.7$, $\alpha_2 = -0.2$. **b.** HPAM 1000 ppm: $\alpha_1 = 0.46$, $\alpha_2 = -0.02$. **c.** HPAM 200 ppm: $\alpha_1 = 4.10^{-4}$, $\alpha_2 = -3.10^{-5}$. **d.** Comparison of the integrated pressure from the sensor array $P_{\text{sensors}}$ to the mean pressure given by the built-in force sensor of the rheometer $P_{\text{rheometer}}$. The dotted line has a slope equal to 1.

of the sensors. In Fig. 3a, the rotation axis corresponds to one corner of the middle sensor (as schematised in Fig. 2c), while in the two other cases, the sensor is centered. $m$ is deduced from the best fit of the mean vertical stress $F_z/\pi R^2 = N_1 - N_2$ as a function of $\dot{\gamma}$ (Figure 2b). The slope of the linear plot $P/\dot{\gamma}_R^m = f((r/R)^m)$ gives $-\frac{\alpha_1+(m+1)\alpha_2}{m}$ and the intercept at the origin is $\frac{\alpha_1+\alpha_2}{m}$, from which $\alpha_1$ and $\alpha_2$ are calculated. The error on $\alpha_1$ is typically of the order of 25%, while for $\alpha_2$ (which is one order of magnitude smaller than $\alpha_1$) it is of the order of 100%. The corresponding pressure profiles (with a unique $\alpha_1$ and $\alpha_2$ per concentration) are plotted in Figure 3a-c, with $\alpha_1 = 4.7$ and $\alpha_2 = -0.2$ for $c = 5000$ ppm, $\alpha_1 = 0.46$ and $\alpha_2 = -0.02$ for $c = 1000$ ppm and $\alpha_1 = 4 \times 10^{-4}$ and $\alpha_2 = -3 \times 10^{-5}$ for $c = 200$ ppm. As expected for viscoelastic liquids, $\alpha_1$ is positive and $\alpha_2$ negative, with $|\alpha_1| \gg |\alpha_2|$. Typically, $\alpha_1$ decreases by a factor 10 between the 5000 ppm and the 1000 ppm solutions, and decreases by a factor 1000 when comparing the 1000 ppm to the 200 ppm solutions. Remarkably, we can still measure the normal stress coefficients in the extremely dilute (200 ppm) polymer solution, for which the maximum mean normal stress is smaller than 10 Pa at high shear. To finally check the validity and precision of the sensors, the experimental pressures profiles are integrated to obtain the mean pressure $P_{\text{sensors}}$ over the surface of the geometry. In Figure 3d, $P_{\text{sensors}}$ is compared to the pressure obtained through the built-in sensor of the rheometer $P_{\text{rheometer}}$. The error bars correspond to the pressure detection threshold (taken at 2 Pa for the sensor array and 4 Pa for the rheometer, see Supplementary Figure 2). All the data collapse on a line with slope 1 (indicated with a dotted line), which confirms that the pressure measured by the sensors is fully consistent with the pressure given by the rheometer instruments.

## IV. NEGATIVE PRESSURES MEASUREMENT

The sensors are also sensitive to negative pressures, which can be measured after a calibration in extension. To obtain controlled negative pressures, we use the same method than Adams [2], or, more recently, by Dbouk [14]. We take advantage of the fact that the flow in a parallel plate geometry is not purely viscosimetric. Even at small Reynolds numbers, there is always a small recirculation because of inertia [14, 41–43] (this appears in the term $\frac{\partial p}{\partial r}$ in Eq. 1.) This secondary flow consists of an inward motion, close to the plate, and an outward motion, near the rotating disk which pulls the plate and the rotating disk together. The effect of the recirculation on the rheology curves is presented in Figure 4a, for a Newtonian fluid (a mixture of 98% glycerol with water), with density $\rho = 1250$ kg/m$^3$ and viscosity $\eta = 0.74$ Pa s at 22°C. Usually, at low angular velocities, this secondary flow does not disturb the viscosity measurements. It simply induces a positive total normal stress on the plate, which corresponds to a negative pressure $P$. However, depending on the value of the Laplace pressure in the meniscus, it may be at the origin of liquid ejection. This phenomenon is observed in our experiment at high shear rates $\dot{\gamma} > 200$ s$^{-1}$: the ejection of a small amount of liquid comes with a decrease of the viscosity - which differs from the constant value expected for a purely Newtonian fluid (dotted line). Note that if the liquid were wetting, the ejection would occur at higher shear rate. In this situation, the recirculation might induced an increase of the viscous loss and the measurement of an effective viscosity increasing with the shear rate [43]. This ejection, however, does not modify the normal pressure on our small sensors, since they are at least 3 mm away from the meniscus.

What is to interest for us here is that the recirculation generates a negative pressure $P$ in the fluid, which absolute amplitude increases with $\Omega$. This pressure is large enough to be detected by the sensor of the rheometer, as visible in blue in Figure 4a. The pressure profile generated by the recirculation is found to vary quadratically with both the angular velocity $\Omega$ and with the distance $r$ to the center of the geometry. Following [41–43], the exact expression of $P$ is:

$$P(r) = -\frac{3}{20}\rho\Omega^2(R^2 - r^2). \tag{5}$$

so that the mean theoretical pressure (averaged over the surface $S = \pi R^2$ of the geometry) writes: $P_\Omega = -3/40\rho R^2\Omega^2$. This prediction is shown in Figure 4a with a blue dotted line, and compared with the experiment (blue triangles). The model reproduces well the decrease of $P_\Omega$ for $\dot{\gamma} > 200$ s$^{-1}$. This indicates that the effect of inertia on the meniscus and the potential fluid loss (visible in the viscosity measurement)

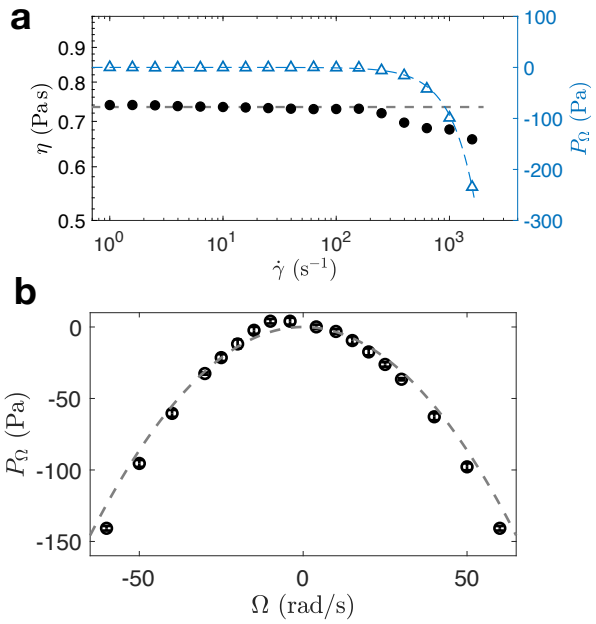


FIG. 4. **a.** Viscosity $\eta$ and mean normal stress (measured by the force sensor of the rheometer) of a 98% glycerol solution in water as a function of $\dot{\gamma}$. A value of $\dot{\gamma} = 200$ s$^{-1}$ corresponds to an angular velocity $\Omega$ = 10 rad/s in this geometry. **b.** Mean normal pressure $P_\Omega$ measured through the force sensor of the rheometer, as a function of the rotor angular velocity $\Omega$. The dotted lines are the parabolic fits expected from the theory.

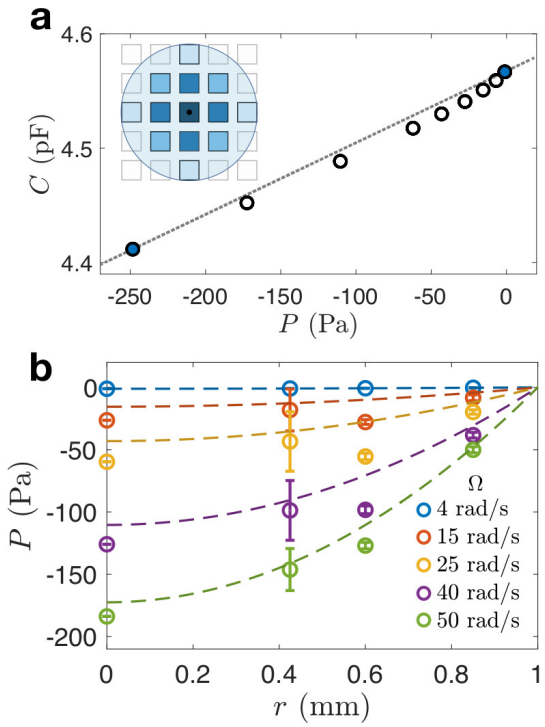


FIG. 5. **a.** Calibration curve of a sensor, with (in dotted line) a linear fit. **b.** Radial distribution of the pressure in a parallel plate torsional flow, for varying angular velocities $\Omega$.

remains of second order compared with the effect of the recirculation on the pressure measurements. The parabolic shape of $P_\Omega$ is even more clearly visible when plotted in a linear scale, as presented in Figure 4b. In this experiment, the angular velocity $\Omega$ is varied between -60 rad/s and 60 rad/s: in this range of velocities, the experiment and model nicely overlap.

In the following, we use this negative pressure profile to calibrate the sensors in extension, and to test them in a configuration where $P < 0$. As presented in the inset of Figure 5a, the sensor array is here centered with respect to the geometry. The pressure $P$ is measured at four different distances $r$ from the center of the geometry. The sensors are calibrated by measuring their capacitance at two extreme angular velocities: $\Omega = 0$ and $\Omega = 60$ rad/s, and the corresponding pressure is deduced from Eq. 5. A linear interpolation between these two extreme points is sufficient here to calibrate the sensors. As presented in Figure 5a, the sensor capacitance $C$ varies almost linearly with $P$ in the region of negative pressures considered (-300 Pa $< P <$ 0 Pa). The dotted line shows the linear interpolation between the extrema (blue points): it fits convincingly all intermediate measurements (black circles).

After calibration, we test the validity of our sensors to measure negative pressures. To do so, we compare the pressure profiles $P(r)$ measured experimentally to the theory, for varying angular velocities $\Omega$ (4 rad/s $< \Omega <$ 50 rad/s). In Figure 5b, the experimental results are shown in circles, with a different color for each $\Omega$. The error bars show the difference in pressure measured by different sensors placed at an equal distance $r$ from the center. The pressure profiles $P(r)$ are quadratic, as expected from Equation 5. The theoretical profile is presented with a dotted line: it compares well with the experimental measurements. This demonstrates that the sensors arrays also detect negative pressures with a reasonable accuracy. In the following, the pressure measurement in an inertial Newtonian fluid flow will be used as a reference flow to calibrate the sensors for negative pressures.

## V. EVIDENCING HETEROGENEITIES

Interestingly, the small size of the sensors when compared with the size of the geometry, combined with a high measurement frequency, make them a very good tool to study heterogeneous flows. We consider here a suspension of non-Brownian solid particles (of cornstarch) in a neutrally buoyant Newtonian liquid. At high solid fractions $\phi$, these suspensions exhibit a striking shear-thickening behavior: while they flow easily at low stirring, they become highly viscous at high stirring with an almost solid-like behavior. It is now admitted that this shear-thickening phenomenon associated with an evolution from a lubricated interaction between the particles (at low shear) to a frictional contact (at high shear), due to an increase of the normal stresses that push particles together [44–49]. Interestingly, close to the shear-thickening transition, large temporal fluctuations in viscosity, shear rate or density are often observed in shear thickening fluids, including cornstarch [50–52]. Recent experiments and new measure-

ment methods (magnetic resonance [53], ultrasound imaging [54], X-ray radiography [21] or boundary stress microscopy [55]) seem to indicate that these fluctuations are associated with an heterogeneous flow. This observation is further confirmed by recent simulations [56], but a lot remain to be understood, still, on the nature of the heterogeneities and their origin. Even if they seem to be consistently observed in some shear thickening systems, is also not clear whether all shear thickening fluids become heterogeneous.

We use here a suspension of solid cornstarch particles, a popular shear-thickening system [20, 54]. The solid particles are put in an isodensity salt of CsCl in water (55% w/w of CsCl). Here, we use a suspension of 41% in weight of cornstarch, as done in Refs [21, 54] so that the fluid is in the discontinuous shear-thickening region. In Figure 6a, the viscosity of the 41% in weight cornstarch suspension is measured as a function of $\dot{\gamma}$, for stress steps of 60 s. At this weight fraction of 41%, cornstarch is shear-thinning at low shear rate ($\dot{\gamma} < 2$ s$^{-1}$) and strongly shear thickening above a critical shear rate $\dot{\gamma}_c = 5$ s$^{-1}$, with a viscosity $\eta$ increasing by more than one order of magnitude. In figure 6b, we report the mean normal stress generated by the flow as recorded by the rheometer. Here again, two regions can be distinguished: at low shear rates, normal stresses are small and negative and decrease slowly with $\dot{\gamma}$. For a shear rate $\dot{\gamma} > 15$ s$^{-1}$, however, normal stresses become positive and increase rapidly with $\dot{\gamma}$. The error bars indicate the amplitude of the pressure fluctuations, which increase dramatically in the shear-thickening region.

To the best of our knowledge, the sensor arrays presented in this work (accounting for normal stresses associated with fluctuations) have not been presented in the literature so far. We use here two sensors, placed at opposite directions below the rotating plate, at an identical distance $r = 12$ mm from the center (see the inset of Figure 6c). They record the pressure at a high frequency of 100 Hz. To study the dynamical behavior of the suspension, we impose steps of constant shear stress $\sigma$ of 300 s, either in the shear-thinning region ($\sigma$ = 1 and 5 Pa) or in the shear-thickening region ($\sigma$ = 20, 100 and 150 Pa). These points are highlighted by colored circles in Figure 6a and b. We observe that the measurements corresponding to the 300 s steps coincide with the 60 s measurements, contrary to what was observed in other shear thickening suspensions [21]. We explain this by the combination of a limited particle migration in parallel-plate geometries [57, 58] and the relatively short timescale of the experiment.

In Figures 6c-f, we report the pressures measured by the two diagonal sensors (in blue and orange) as a function of time, for each stress step. The typical response of the central sensor is also shown in Supplementary Figure 6. For $\sigma = 5$ Pa, below the discontinuous shear-thickening region, the pressure is constant and identical for both sensors (figure 6c). It is slightly negative ($P \simeq -10 \pm 3$ Pa, see zoom in the inset), in good agreement with the global pressure measured by the rheometer. However, just after the shear thickening region is reached, oscillations become visible. The pressure variations are initially small, of the order of 30 Pa for $\sigma$ = 20 Pa (see Figure 6 and inset). They increase in amplitude with increasing $\sigma$: the pressure variation is of the order of 150 Pa for $\sigma$ = 100 Pa and 350 Pa for $\sigma = 150$ Pa. Very interestingly, the pressure fluctuations are extremely regular, with out of phase peaks of similar amplitude and a constant negative pressure in between. The period $T$ between two peaks slightly decreases with increasing shear stress $\sigma$: $T$ = 15.1 s, 13.3 s and 11.3 s respectively for $\sigma = 20, 100$ and 150 Pa. Interestingly, $T$ is very close to twice the rotational period of the upper disk (respectively equal to 13.8, 11.3 and 10.7 s). All these results seem to indicate the presence of one large aggregate rotating with a angular velocity $\Omega_A \simeq \Omega/2$ within the parallel plate geometry. The presence of this aggregate is associated with local and very high normal stresses: for $\sigma = 150$ Pa, the peak pressure is 7 times higher than the mean pressure obtained through the force sensor of the rheometer.

This observation is in good agreement with the recent work of Ovarlez *et al.*, which evidenced the presence of "density waves" in a similar cornstarch suspension [21]. In a Couette cell, the density waves move in the flow direction, more slowly than the rotor, similarly to what is detected here. Our results are also consistent with the observations of Rathee *et al.* [55], who showed the presence of zones of high shear stress propagating with an angular velocity $\Omega_A = \Omega/2$ in a suspension of sub-micronic silica particles in glycerol. Here, for the first time, we evidence and measure the normal stresses associated with these heterogeneities. The stresses measured by the sensors are 5 to 10 times higher than the average pressure obtained through the rheometer. The asymmetric forces surely generate a large torque on the geometry, and are thus most likely at the origin of the off-axis motion of the rotor in Couette cells. This phenomenon has been observed so far in cornstarch [21] and in latex particle suspensions [59]. It should be noted, finally, that even in a simple parallel plate geometry, the amplitude of the peak pressure remains undetected by the force sensor of the rheometer: the fluctuations are only visible when measured over an area significantly smaller than the plate size to avoid a compensation between the low and high pressure regions.

## VI. CONCLUSION

In the study of Newtonian fluids or homogeneous flows, conventional rheometers, which give access to the average values of the shear stress and normal forces, are particularly relevant. However, heterogeneous flows often occur in complex fluids, as in cornstarch suspensions. The sensor array that we present here is a new tool that brings a new insight into these flows. Here, we access to $\sigma_{22}$ = -$\sigma_{zz}$, an important parameter that is much less studied than the shear components of the stress tensor. Our results evidence the potential of the sensor array, not only to measure the normal stresses $N_1$ and $N_2$ (as done with the HPAM solution) but to evidence and follow heterogeneities (as in cornstarch suspensions). It is, to our knowledge, the only sensor capable of evidencing the normal stresses generated by rapidly moving objects, with very high signal to noise and with a frequency up to 200 Hz. In addition, and in contrast with other pressure sensors, our system is highly versatile. The size, number and position of the sen-

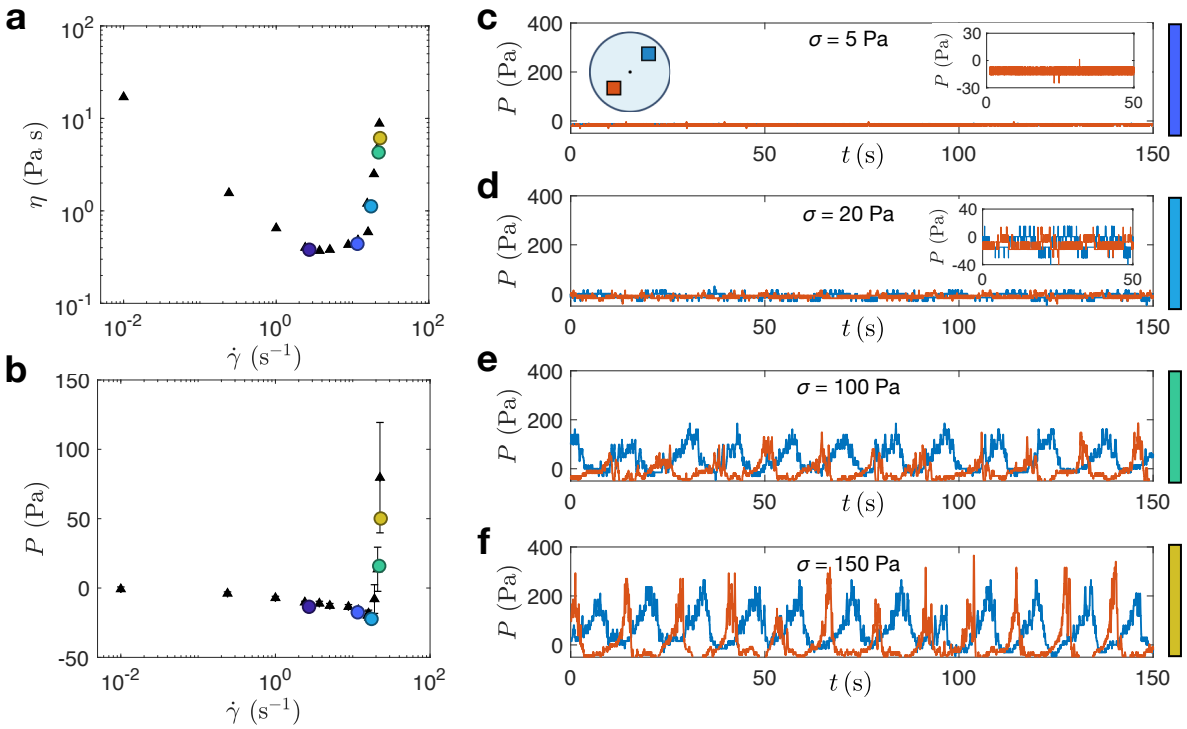


FIG. 6. Suspension of 41% of cornstarch particles in an isodensity water/CsCl solution. **a.** Viscosity $\eta$ as a function of the shear stress $\dot{\gamma}$. **b.** Normal stress $P$ measured by the axis of the rheometer as a function of $\dot{\gamma}$. **c-f.** Normal stress measurement of the sensors as a function of time, for varying imposed constant stresses $\sigma$. Two 4x4 mm$^2$ sensors (in red and blue see inset of **c**) are placed in opposite directions on a diagonal. **c.** $\sigma$ = 5 Pa. **d.** $\sigma$ = 20 Pa. **e.** $\sigma$ = 100 Pa. **f.** $\sigma$ = 150 Pa.

sors can be modified by replacing the bottom electrode array, which is independent from the measurement surface.
Further developments are also possible: the addition of a soft bottom electrode would make the whole sensor array bendable enough to be added to a Couette geometry. The measurement of normal stresses has never been reported in this very common geometry, despite a huge interest of the community. It would very nicely complement the experiments (of X ray radiography or ultrasound imaging) that have been previously made in such a geometry [21, 54] with heterogeneous flows.

## SUPPLEMENTARY MATERIAL

See the supplementary material to access Supplementary Figures 1 to 6 and for a second method for the measurement of $N_1$ and $N_2$ using the same sensors.


[1] Robert Byron Bird, Robert C Armstrong, and Ole Hassager. *Dynamics of polymeric liquids. Vol. 1: Fluid mechanics*. Wiley, 1987.

[2] N Adams and AS Lodge. Rheological properties of concentrated polymer solutions ii. a cone-and-plate and parallel-plate pressure distribution apparatus for determining normal stress differences in steady shear flow. *Philosophical Transactions of the Royal Society of London. Series A, Mathematical and Physical Sciences*, 256(1068):149–184, 1964.

[3] M Keentok, AG Georgescu, AA Sherwood, and RI Tanner. The measurement of the second normal stress difference for some polymer solutions. *Journal of Non-Newtonian Fluid Mechanics*, 6(3-4):303–324, 1980.

[4] HW Gao, S Ramachandran, and EB Christiansen. Dependency of the steady-state and transient viscosity and first and second normal stress difference functions on molecular weight for linear mono and polydisperse polystyrene solutions. *Journal of Rheology*, 25(2):213–235, 1981.

[5] J Meissner, RW Garbella, and J Hostettler. Measuring normal stress differences in polymer melt shear flow. *Journal of Rheology*, 33(6):843–864, 1989.

[6] Thomas Schweizer. Measurement of the first and second normal stress differences in a polystyrene melt with a cone and partitioned plate tool. *Rheologica acta*, 41(4):337–344, 2002.

[7] Mataz Alcoutlabi, SG Baek, JJ Magda, Xiangfu Shi, SA Hutcheson, and GB McKenna. A comparison of three different methods for measuring both normal stress differences of viscoelastic liquids in torsional rheometers. *Rheologica acta*, 48(2):191–200, 2009.

[8] Alberto Montesi, Alejandro A Pena, and Matteo Pasquali. Vorticity alignment and negative normal stresses in sheared attractive emulsions. *Physical review letters*, 92(5):058303, 2004.

[9] Jyoti R Seth, Lavanya Mohan, Clémentine Locatelli-Champagne, Michel Cloitre, and Roger T Bonnecaze. A micromechanical model to predict the flow of soft particle glasses. *Nature materials*, 10(11):838–843, 2011.

[10] Henri De Cagny, Mina Fazilati, Mehdi Habibi, Morton M Denn, and Daniel Bonn. The yield normal stress. *Journal of Rheology*, 63(2):285–290, 2019.

[11] Isidro E Zarraga, Davide A Hill, and David T Leighton Jr. The characterization of the total stress of concentrated suspensions of noncolloidal spheres in newtonian fluids. *Journal of Rheology*, 44(2):185–220, 2000.

[12] Étienne Couturier, François Boyer, Olivier Pouliquen, and Élisabeth Guazzelli. Suspensions in a tilted trough: second normal stress difference. *Journal of Fluid Mechanics*, 686:26–39, 2011.

[13] Shao-Cong Dai, Erwan Bertevas, Fuzhong Qi, and Roger I Tanner. Viscometric functions for noncolloidal sphere suspensions with newtonian matrices. *Journal of Rheology*, 57(2):493–510, 2013.

[14] Talib Dbouk, Laurent Lobry, and Elisabeth Lemaire. Normal stresses in concentrated non-brownian suspensions. *Journal of Fluid Mechanics*, 715:239–272, 2013.

[15] Romain Mari, Ryohei Seto, Jeffrey F Morris, and Morton M Denn. Shear thickening, frictionless and frictional rheologies in non-brownian suspensions. *Journal of Rheology*, 58(6):1693–1724, 2014.

[16] Laurent Lobry, Elisabeth Lemaire, Frédéric Blanc, Stany Gallier, and François Peters. Shear thinning in non-brownian suspensions explained by variable friction between particles. *Journal of Fluid Mechanics*, 860:682–710, 2019.

[17] François Boyer, Olivier Pouliquen, and Élisabeth Guazzelli. Dense suspensions in rotating-rod flows: normal stresses and particle migration. *Journal of Fluid Mechanics*, 686:5–25, 2011.

[18] Matti Keentok and Shi-Cheng Xue. Edge fracture in cone-plate and parallel plate flows. *Rheologica acta*, 38(4):321–348, 1999.

[19] Roger I Tanner and Shaocong Dai. Edge fracture in non-colloidal suspensions. *Journal of Non-Newtonian Fluid Mechanics*, 272:104171, 2019.

[20] Abdoulaye Fall, N Huang, François Bertrand, G Ovarlez, and Daniel Bonn. Shear thickening of cornstarch suspensions as a reentrant jamming transition. *Physical Review Letters*, 100(1):018301, 2008.

[21] Guillaume Ovarlez, Ahn Vu Nguyen Le, Wilbert J Smit, Abdoulaye Fall, Romain Mari, Guillaume Chatté, and Annie Colin. Density waves in shear-thickening suspensions. *Science Advances*, 6:eaay5589, 2020.

[22] RF Ginn and AB Metzner. Measurement of stresses developed in steady laminar shearing flows of viscoelastic media. *Transactions of the Society of Rheology*, 13(4):429–453, 1969.

[23] Roger I Tanner and Shaocong Dai. Particle roughness and rheology in noncolloidal suspensions. *Journal of Rheology*, 60(4):809–818, 2016.

[24] GS Beavers and DD Joseph. The rotating rod viscometer. *Journal of Fluid Mechanics*, 69(3):475–511, 1975.

[25] JJ Magda, Jianzhong Lou, SG Baek, and KL De Vries. Second normal stress difference of a boger fluid. *Polymer*, 32(11):2000–2009, 1991.

[26] RI Tanner. Some methods for estimating the normal stress functions in viscometric flows. *Transactions of the Society of Rheology*, 14(4):483–507, 1970.

[27] MJ Miller and EB Christiansen. The stress state of elastic fluids in viscometric flow. *AIChE Journal*, 18(3):600–608, 1972.

[28] Seong-Gi Baek and Jules J Magda. Monolithic rheometer plate fabricated using silicon micromachining technology and containing miniature pressure sensors for $n_1$ and $n_2$ measurements. *Journal of Rheology*, 47(5):1249–1260, 2003.

[29] Roger I Tanner and AC Pipkin. Intrinsic errors in pressure-hole measurements. *Transactions of the Society of Rheology*, 13(4):471–484, 1969.

[30] WG Pritchard. The measurement of normal stresses by means of liquid-filled holes in a surface. *Rheologica Acta*, 9(2):200–207, 1970.

[31] Mickael Pruvost, Wilbert J Smit, Cécile Monteux, Philippe Poulin, and Annie Colin. Microporous electrostrictive materials for vibrational energy harvesting. *Multifunctional Materials*, 1(1):015004, 2018.

[32] Mickael Pruvost, Wilbert J Smit, Cécile Monteux, Philippe Poulin, and Annie Colin. Polymeric foams for flexible and highly sensitive low-pressure capacitive sensors. *npj Flexible Electronics*, 3(1):1–6, 2019.

[33] Ewan J Hemingway, Halim Kusumaatmaja, and Suzanne M Fielding. Edge fracture in complex fluids. *Physical review letters*, 119(2):028006, 2017.

[34] Durgesh Kawale, Esteban Marques, Pacelli LJ Zitha, Michiel T Kreutzer, William R Rossen, and Pouyan E Boukany. Elastic instabilities during the flow of hydrolyzed polyacrylamide solution in porous media: effect of pore-shape and salt. *Soft matter*, 13(4):765–775, 2017.

[35] Hugues Bodiguel, Julien Beaumont, Anaïs Machado, Laetitia Martinie, Hamid Kellay, and Annie Colin. Flow enhancement due to elastic turbulence in channel flows of shear thinning fluids. *Physical review letters*, 114(2):028302, 2015.

[36] Guice Yao, Haie Yang, Jin Zhao, and Dongsheng Wen. Experimental study on flow and heat transfer enhancement by elastic instability in swirling flow. *International Journal of Thermal Sciences*, 157:106504, 2020.

[37] Peyman Pakdel and Gareth H McKinley. Elastic instability and curved streamlines. *Physical Review Letters*, 77(12):2459, 1996.

[38] Gareth H McKinley, Peyman Pakdel, and Alparslan Öztekin. Rheological and geometric scaling of purely elastic flow instabilities. *Journal of Non-Newtonian Fluid Mechanics*, 67:19–47, 1996.

[39] RG Larson, SJ Muller, and ESG Shaqfeh. The effect of fluid rheology on the elastic taylor-couette instability. *Journal of non-newtonian fluid mechanics*, 51(2):195–225, 1994.

[40] Susan J Muller. Elastically-influenced instabilities in taylor-couette and other flows with curved streamlines: a review. *Korea-Australia Rheology Journal*, 20(3):117–125, 2008.

[41] JG Savins and AB Metzner. Radial (secondary) flows in rheogoniometric devices. *Rheologica Acta*, 9(3):365–373, 1970.

[42] DH McCoy and MM Denn. Secondary flow in a parallel-disk viscometer. *Rheologica Acta*, 10(3):408–411, 1971.

[43] Raffi M Turian. Perturbation solution of the steady newtonian flow in the cone and plate and parallel plate systems. *Industrial & Engineering Chemistry Fundamentals*, 11(3):361–368, 1972.

[44] Matthieu Wyart and ME Cates. Discontinuous shear thickening without inertia in dense non-brownian suspensions. *Physical review letters*, 112(9):098302, 2014.

[45] Ryohei Seto, Romain Mari, Jeffrey F Morris, and Morton M Denn. Discontinuous shear thickening of frictional hard-sphere suspensions. *Physical review letters*, 111(21):218301, 2013.

[46] Nicolas Fernandez, Roman Mani, David Rinaldi, Dirk Kadau, Martin Mosquet, Hélene Lombois-Burger, Juliette Cayer-Barrioz, Hans J Herrmann, Nicholas D Spencer, and Lucio Isa.

Microscopic mechanism for shear thickening of non-brownian suspensions. *Physical review letters*, 111(10):108301, 2013.

[47] BM Guy, Michiel Hermes, and Wilson CK Poon. Towards a unified description of the rheology of hard-particle suspensions. *Physical review letters*, 115(8):088304, 2015.

[48] John R Royer, Daniel L Blair, and Steven D Hudson. Rheological signature of frictional interactions in shear thickening suspensions. *Physical review letters*, 116(18):188301, 2016.

[49] Cécile Clavaud, Antoine Bérut, Bloen Metzger, and Yoël Forterre. Revealing the frictional transition in shear-thickening suspensions. *Proceedings of the National Academy of Sciences*, 114(20):5147–5152, 2017.

[50] Didier Lootens, Henri Van Damme, and Pascal Hébraud. Giant stress fluctuations at the jamming transition. *Physical review letters*, 90(17):178301, 2003.

[51] Matthias Grob, Annette Zippelius, and Claus Heussinger. Rheological chaos of frictional grains. *Physical Review E*, 93(3):030901, 2016.

[52] Michiel Hermes, Ben M Guy, Wilson CK Poon, Guilhem Poy, Michael E Cates, and Matthieu Wyart. Unsteady flow and particle migration in dense, non-brownian suspensions. *Journal of Rheology*, 60(5):905–916, 2016.

[53] Abdoulaye Fall, François Bertrand, David Hautemayou, Cédric Méziere, Pascal Moucheront, Anael Lemaitre, and Guillaume Ovarlez. Macroscopic discontinuous shear thickening versus local shear jamming in cornstarch. *Physical review letters*, 114(9):098301, 2015.

[54] Brice Saint-Michel, Thomas Gibaud, and Sébastien Manneville. Uncovering instabilities in the spatiotemporal dynamics of a shear-thickening cornstarch suspension. *Physical Review X*, 8(3):031006, 2018.

[55] Vikram Rathee, Daniel L Blair, and Jeffrey S Urbach. Localized stress fluctuations drive shear thickening in dense suspensions. *Proceedings of the National Academy of Sciences*, 114(33):8740–8745, 2017.

[56] Rahul N Chacko, Romain Mari, Michael E Cates, and Suzanne M Fielding. Dynamic vorticity banding in discontinuously shear thickening suspensions. *Physical review letters*, 121(10):108003, 2018.

[57] Ju Min Kim, Song Geun Lee, and Chongyoup Kim. Numerical simulations of particle migration in suspension flows: Frame-invariant formulation of curvature-induced migration. *Journal of Non-Newtonian Fluid Mechanics*, 150(2-3):162–176, 2008.

[58] Dima Merhi, Elisabeth Lemaire, Georges Bossis, and Fadl Moukalled. Particle migration in a concentrated suspension flowing between rotating parallel plates: Investigation of diffusion flux coefficients. *Journal of Rheology*, 49(6):1429–1448, 2005.

[59] H.M.Laun. Normal stresses in extremely shear thickening polymer dispersions. *J.Nonnewton. Fluid Mech.*, 54:87–108, 1994.